Near-perfect broadband absorption from hyperbolic metamaterial nanoparticles

Conor T. Riley[a], Joseph S. T. Smalley[b], Jeffrey R. J. Brodie[a], Yeshaiahu Fainman[b,c], Donald J. Sirbuly[a,c,1], and Zhaowei Liu[b,c,1]

[a]Department of NanoEngineering, University of California, San Diego, La Jolla, CA 92093; [b]Department of Electrical and Computer Engineering, University of California, San Diego, La Jolla, CA 92093; and [c]Materials Science and Engineering, University of California, San Diego, La Jolla, CA 92093

Edited by Mikhail A. Kats, University of Wisconsin, Madison, WI, and accepted by Editorial Board Member Evelyn L. Hu December 22, 2016 (received for review August 9, 2016)

Broadband absorbers are essential components of many light detection, energy harvesting, and camouflage schemes. Current designs are either bulky or use planar films that cause problems in cracking and delamination during flexing or heating. In addition, transferring planar materials to flexible, thin, or low-cost substrates poses a significant challenge. On the other hand, particle-based materials are highly flexible and can be transferred and assembled onto a more desirable substrate but have not shown high performance as an absorber in a standalone system. Here, we introduce a class of particle absorbers called transferable hyperbolic metamaterial particles (THMMP) that display selective, omnidirectional, tunable, broadband absorption when closely packed. This is demonstrated with vertically aligned hyperbolic nanotube (HNT) arrays composed of alternating layers of aluminum-doped zinc oxide and zinc oxide. The broadband absorption measures >87% from 1,200 nm to over 2,200 nm with a maximum absorption of 98.1% at 1,550 nm and remains large for high angles. Furthermore, we show the advantages of particle-based absorbers by transferring the HNTs to a polymer substrate that shows excellent mechanical flexibility and visible transparency while maintaining near-perfect absorption in the telecommunications region. In addition, other material systems and geometries are proposed for a wider range of applications.

hyperbolic metamaterials | perfect absorber | nanoparticle | nanowire | photonic hypercrystal

Selective and broadband perfect absorbers generally consist of plasmonic cavities coupled to metallic reflectors separated by dielectric spacers. These geometries have led to many exciting applications such as thermophotovoltaics (TPV) (1, 2), thermal emitters (3, 4), camouflage (5), and thermal detectors (6). However, the ability to be scaled up to larger surface area devices and transferred to more desirable substrates is a major limitation of absorbers that rely on planar reflectors. Here, we introduce a class of standalone particles, transferrable hyperbolic metamaterial particles (THMMP), that display broadband, selective, omnidirectional absorption and can be transferred to secondary substrates, allowing enhanced flexibility and selective transmission. This is demonstrated using vertically aligned hyperbolic metamaterial nanotube (HNT) arrays. We first realize the concept by fabricating the HNTs on silicon substrates and then transfer the arrays to a thin elastomer to create a mechanically flexible, visibly transparent material that maintains near-perfect absorption at telecommunication wavelengths (~1,550 nm). In addition, different materials systems and geometries are discussed, leading to a broader range of applications.

Currently, carbon nanotubes (CNTs) provide perfect ultrabroadband absorption (7). However, CNT films are relatively thick and do not allow any control over the operating wavelengths of the absorber, which is critical for creating visibly transparent IR absorbers and materials for many other applications including TPV that require selective yet broadband absorption (8). Hyperbolic metamaterials (HMMs) can provide an alternative to creating selective and broadband absorption. HMMs are materials engineered to possess extreme optical anisotropy that is typically observed and studied in two structures: (*i*) alternating layers of metal and dielectrics and (*ii*) metallic nanowires embedded in a dielectric medium (9, 10). In each case, the characteristic dimensions (layer thickness or nanowire diameter and separation distance) must be deeply subwavelength such that the bulk material properties can be described under an effective medium approximation (EMA), where the permittivity is defined in terms of a tensor with one unique axis (optical axis) and two similar axes. When the optical axis has an opposing sign to the other two axes, the material dispersion is hyperbolic, arising from a hyperboloidal isofrequency surface (9). This stands in contrast to the ellipsoidal isofrequency surface of conventional materials. The hyperbolic dispersion results in an extremely large optical density of states that supports large wavevector modes. This property has been used to exploit negative refraction (11–13), enhanced spontaneous emission (14), and hyperlensing (15).

Due to the large optical density of states, layered HMMs have been shown to be excellent absorbers within narrowbands (16, 17). It has also been shown that the absorption bandwidth could be increased yet still remain selective by structuring the HMMs into pyramids (18–20); however, these materials have shown limited absorption at telecommunication wavelengths (~85%), have not yet shown large-angle absorption, and have only been demonstrated on metallic back reflectors, making simultaneous broadband absorbance and visible transparency challenging.

Significance

The ability to perfectly absorb light with optically thin materials poses a significant challenge for many applications such as camouflage, light detection, and energy harvesting. Current designs require planar reflectors that crack and delaminate after heating or flexing. Moreover, they cannot be transferred to more desirable substrates for mechanically flexible and low-cost applications. Although particulate-based materials overcome these challenges, broadband absorption from standalone systems has not been demonstrated. Here, a class of materials, transferrable hyperbolic metamaterial particles (THMMP), is introduced. When closely packed, these materials show broadband, selective, omnidirectional, perfect absorption. This is demonstrated with nanotubes made on a silicon substrate that exhibit near-perfect absorption at telecommunication wavelengths even after being transferred to a mechanically flexible, visibly transparent polymer.

Author contributions: C.T.R., D.J.S., and Z.L. designed research; C.T.R., J.S.T.S., and J.R.J.B. performed research; Y.F. contributed new reagents/analytical tools; and C.T.R., J.S.T.S., D.J.S., and Z.L. wrote paper.

The authors declare no conflict of interest.

This article is a PNAS Direct Submission. M.A.K. is a Guest Editor invited by the Editorial Board.

[1]To whom correspondence may be addressed. Email: zhaowei@ucsd.edu or dsirbuly@ucsd.edu.

This article contains supporting information online at www.pnas.org/lookup/suppl/doi:10.1073/pnas.1613081114/-/DCSupplemental.

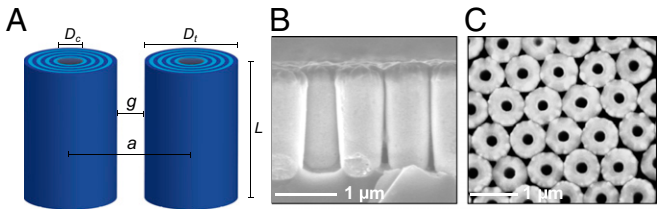

Fig. 1. (*A*) Schematic of coupled HNTs. SEM images of the HNT arrays as viewed in the plane (*B*) parallel and (*C*) perpendicular to the nanotube axis.

Furthermore, the recently demonstrated HMM pyramids are made with low–melting-point metals that are not compatible with the high temperatures required for applications such as thermal emitters. Perfect absorbing metamaterials have also been used to demonstrate broadband absorption by the convolution of multiple loss mechanisms (8). However, these materials require dielectric spacers and metallic back reflectors, and use advanced nanostructured geometries, making it difficult to scale up the fabrication for larger area applications and/or transfer the materials to more desirable substrates. More favorable architectures include nanoparticle monolayers and vertically aligned nanowires that can be assembled and transferred via inexpensive techniques to different substrates while maintaining mechanical flexibility due to the gaps between the independent structures (21, 22). In addition, the substrate/nanoparticle interfacial surface area is reduced, mitigating problems that arise due to lattice mismatch. This is particularly important for high-temperature applications such as heat-generating absorbers and thermal emitters, which put extreme stresses on the interfaces within the device.

Hyperbolic Nanotubes

As shown in Fig. 1*A*, an HNT is defined in terms of its length, L; total diameter, D_t; and air core diameter, D_c. The shell is comprised of n HMM periods with alternating aluminum-doped zinc oxide (AZO) and ZnO concentric layers of thicknesses t_m and t_d, respectively. Therefore, one period has a thickness, p, equal to $t_m + t_d$, and the total shell thickness is given as the product of n and p. When oriented in an array, the lattice period, a, and HNT gap, g, are also defined, where $a = g + D_t$. To engineer such an array, we leveraged high-quality, ultraconformal AZO/ZnO HMM multilayers afforded by atomic layer deposition (ALD), which have been shown to display negative refraction due to hyperbolic dispersion (23). The HNT array fabrication starts with a silicon hole array template made by nanosphere lithography. The hole arrays are then filled with the HMM multilayers by exploiting the ultraconformal properties of ALD. Next, reactive ion etching (RIE) is used to remove the top layers and expose the underlying silicon. The silicon surrounding the HNTs is then removed by RIE, leaving a vertically aligned triangular array of closely packed HNTs (see Fig. S1, *Supporting Information*, for the complete fabrication flow). The air core is an artifact of the conformality limit of ALD and/or bowing effects due to imperfect etching profiles in the nanohole template. This can be mitigated by adjusting the ALD and etching parameters; however, the air core has little consequence on the absorption when D_c is ∼220 nm (*Supporting Information*). Fig. 1 *B* and *C* shows the resulting vertically aligned HNTs with D_c, a, and L equal to 235, 770, and 1,730 nm, respectively. D_t varies from 770 nm at the top to 650 nm at the bottom.

Absorption Measurements

It is well documented that the carrier concentration of AZO is dependent on the ALD deposition temperature, T_d, allowing for the absorption of the HNT array to be tuned (24–27). Using an integrating sphere, Fig. 2*A* captures the true absorption spectrum [absorption(%) = 100% − transmission(%) − reflection(%)] of HNT arrays deposited at a T_d of 200 and 185 °C. Broadband absorption of >87% from 1,200 nm to over 2,200 nm is demonstrated with a maximum absorption of 98.1% at 1,550 nm for a T_d of 200 °C. For a T_d of 185 °C, broadband absorption of >87% is observed from 1,500 nm to over 2,200 nm with a maximum absorption of 96.3% at 1,700 nm. As a control, pure AZO nanotubes are also plotted, which exhibit only a modest absorption maximum of 82.5% at 1,400 nm with a narrow spectral width. The HNTs show excellent selectivity by displaying increased reflection at longer wavelengths (Fig. S2*A*). This is due to an increased impedance mismatch as the real permittivity of AZO becomes increasingly negative at longer wavelengths (23). The angular dependence was also studied by sputtering a 100-nm gold film on the back of the silicon. This allowed only the specular reflectance to be considered when calculating the absorption [absorption(%) = 100% − reflectance(%)]. This method was found to be valid within 1% from 1,500 to 2,400 nm and within 6% from 1,400 to 1,500 nm. However, at wavelengths shorter than 1,400 nm, we found that this method was not accurate due to photon scattering (Fig. S2*B*). As shown in Fig. 2 *C* and *D*, HNTs possess omnidirectional absorption for both transverse-magnetic (TM) and transverse-electric (TE) polarizations. For TM polarization, the absorption is maintained above 85% at all angles and wavelengths measured. For TE polarization, the absorption is diminished at higher angles and longer wavelengths; however, an absorption of >70% is maintained across the measured wavelengths and angles smaller than 50°.

Using the complex permittivity values previously published (23), simulated absorption of over 90% from 1,400 to 2,000 nm agrees well with the experimental data (Fig. S3*A*). Our simulations suggest that the broadband absorption arises from the coalescence of bulk/surface plasmons and lossy modes due to the hyperbolic dispersion of the HNT arrays (Fig. S4, *Supporting Information*). In addition, we find that the absorption of the array does not decrease linearly with the HNT filling fraction, indicating that HNT coupling, and therefore g, plays an important role in the absorption. When a periodic dielectric gap is placed within an HMM, the photonic band structure of the system is expected to be altered due to Bragg scattering, even if the gap is deeply subwavelength. This is known as a photonic hypercrystal (28). Because strong

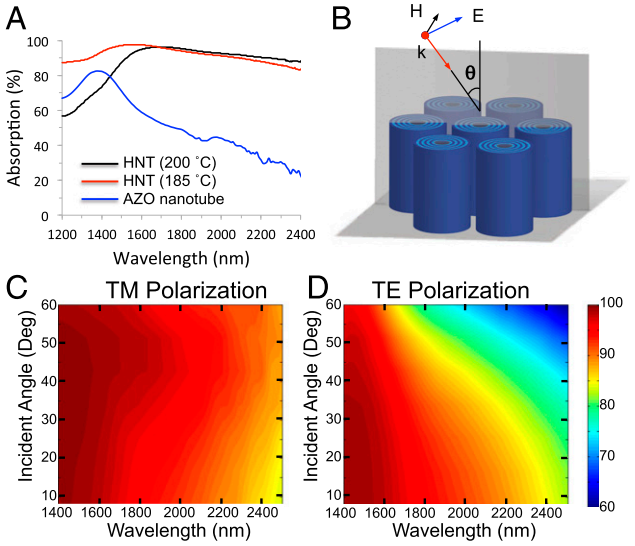

Fig. 2. (*A*) Absorption spectra of HNT arrays deposited at a temperature of 185 and 200 °C along with a spectrum of a pure AZO nanotube array deposited at 200 °C. (*B*) Schematic of the incident radiation at angle θ showing TM polarization. Wide-angle absorption spectra for (*C*) TM and (*D*) TE polarizations of an HNT array deposited at 200 °C. The color corresponds to the percent absorption.

Table 1. Parameters of samples A–C

Sample	L, μm	D_t, nm	D_c, nm	n	t_m, nm	t_d, nm	p, nm	a, nm	g, nm	T_d, °C
A	2.05	700	220	12	10	10	20	770	70	200
B	2.05	700	220	12	10	10	20	770	70	185
C	1.39	620	140	12	10	10	20	770	150	185

coupling provided by periodic dielectric spacing is expected in a THMMP array, the structure can be classified as a photonic hypercrystal. Using a qualitative analytical approach, we observe an alteration in the band structure when adjusting the air gaps for a similar 1D structure in the lossless limit (Figs. S5 and S6, *Supporting Information*). Based on these results, it is clear that the absorption spectrum depends upon both the wavelength-scale periodicity of the hypercrystal and the deeply subwavelength scale of the HMM. The simultaneous control of these structural parameters enables a tailorable absorption and emission spectrum unachievable in other systems, such as self-aligned carbon nanotubes. However, the emission spectrum of quantum emitters has been enhanced recently by embedding them within a photonic hypercrystal where the enhancement is attributed to tailoring the band structure of the high photonic density of state HMM and allowing more efficient coupling into free space (29). Consequently, given the high sensitivity of high wavevector modes to small changes in dielectric spacing, this also suggests that the disorder of the HNT array will likely impact the band structure and thus the absorption properties. However, the incident light from free space typically has small wavevectors, unless a strong scattering effect is present. Therefore, the relationship between disorder-induced high wavevector mode modification and absorption becomes nontrivial. The quantitative analysis of this effect needs further investigation.

Outside of the 1,400- to 2,000-nm spectral range, the experimental absorption is larger than the simulated absorption. The larger observed experimental absorption at wavelengths shorter than 1,400 nm is due to the silicon substrate, as discussed later. At longer wavelengths, this discrepancy is attributed to surface roughness, which is verified both experimentally and by simulation (Fig. S7). It should be noted that, although high absorption has been obtained for planar HMMs (30, 31), our simulations show that the absorption occurs within a narrower band when similar length scales (1.5 μm) are used for both the planar and embedded nanowire HMM geometries (Fig. S8C). Furthermore, planar HMMs do not have the many benefits of nanoparticle films as mentioned above.

HNT Substrate Transfer

To investigate whether the HNT arrays could operate as a standalone material after being removed from the growth substrate, we transferred the arrays to a thin, flexible, and visibly transparent substrate by spin coating 60 μm of polydimethylsiloxane (PDMS) onto the top of the arrays and removing the silicon via RIE. This was carried out for three different arrays with various parameters as described in Table 1 and observed from direct imaging (Fig. S9). The absorption spectra of sample A and a simulated exact structure (with a similar structure to sample A, but with a rounded top to replicate experimental conditions) have excellent agreement (Fig. 3*A*). This suggests that the shorter wavelength discrepancy between the simulated and experimental absorption described earlier is due to the silicon substrate either from reflection back into the HNTs or absorption of the textured surface created during the HNT fabrication. The transmission and absorption spectra of the three samples (Fig. 3 *B* and *C*) illustrate that a large transmission window is observed from 500 to 1,300 nm, with the broadest IR absorption band belonging to sample A at the expense of a narrower and weaker transmission window. The transmission can be slightly increased by lowering T_d and keeping the geometry constant, but the largest gain in transmission is observed when L is decreased and g is increased (sample C). Because all of the constituent materials (AZO, ZnO, and PDMS) in the free-standing HNT array have large optical transparencies throughout the visible, and reflection accounts for <12% of the decreased transparency, we believe the additional absorption stems from silicon contaminates left

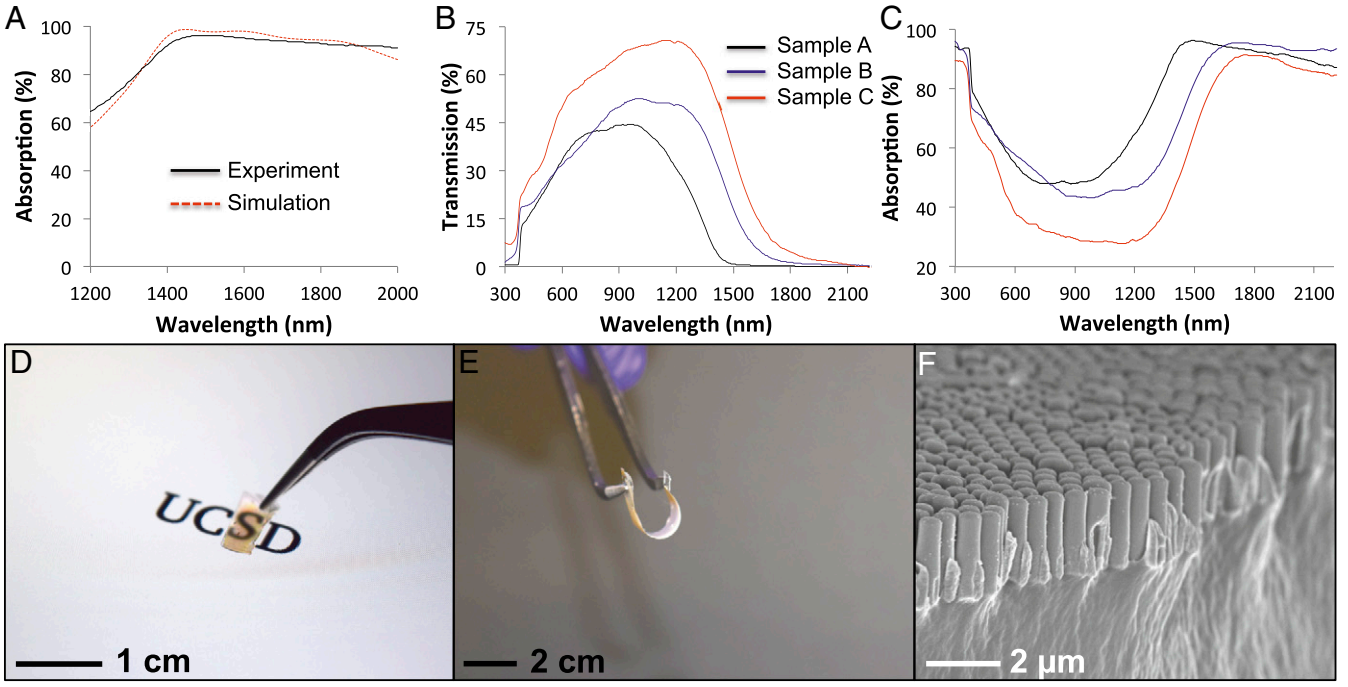

Fig. 3. (*A*) Comparison of experimental and simulated absorption spectra for sample A. (*B*) Transmission and (*C*) absorption spectra for samples A–C with parameters as described in Table 1 after flexing several times as shown in *E*. Photograph of sample A showing (*D*) visible transparency and (*E*) mechanical flexibility. (*F*) SEM image of an HNT array (sample B) after transferring to a flexible PDMS substrate and flexing several times as shown in *E*.

over from the transfer process and/or subband levels (defects states) in the ZnO/AZO layers. With further refinement in the synthesis, etching, and transferring steps, we anticipate a significant improvement in the visible transparency. After transferring the HNT array to the PDMS film, they can be reproducibly flexed while still maintaining their excellent broadband absorption in the near IR (NIR), and transmission in visible, as well as their physical interface with the polymer (Fig. 3 *D*–*F*).

Other THMMP Systems

Beyond the AZO/ZnO HNT system, selective and broadband absorption can be applied to many other material systems and geometries. For example, the TiN/(Al,Sc)N material system has been shown to produce high-quality epitaxial HMMs with refractory qualities (32). THMMP arrays with these materials could be advantageous for applications such as TPV and visible emitters that require many cycles at elevated temperatures (>1,000 °C). Current research in this area focuses on nonselective absorbers (1) and plasmonic metamaterials (8); however, these planar materials either lose efficiency due to parasitic radiation at higher temperatures or can crack and delaminate due to thermal expansion mismatch between the absorber layer and substrate. A major advantage of a THMMP array is that it has a reduced substrate contact area that minimizes the impact of thermal expansion mismatches and would allow for a wider selection of substrates to be used while promoting the use of facile transfer techniques. Simulations reveal that TiN/(Al,Sc)N-based HNT arrays ($L = 750$ nm, $D_t = 500$ nm, $D_c = 30$ nm, $n = 11$, $t_m = t_d = 10$ nm, $a = 530$ nm) have absorption values of >93% throughout the entire visible spectrum while suppressing absorption at longer wavelengths (Fig. S10*A*). In comparison with the HNT geometry, closely packed hyperbolic nanospheres could be particularly useful because they are expected to have less angular dependence and can be deposited onto substrates via low-cost/scalable processes such as nanoparticle self-assembly and spray-on techniques. Simulations also reveal that these types of arrays made from a TiN/(Al,Sc)N material system have a large absorption (>89% throughout the entire visible spectrum) while suppressing absorption in the NIR with only a 540-nm-thick single monolayer (Fig. S10*B*).

Conclusions

In conclusion, we have demonstrated a class of metamaterials, THMMP, that have tunable, selective, and broadband near-perfect, omnidirectional absorption. The broad absorption bandwidth is a result of the coalescence of absorption peaks due to bulk or surface plasmon-polaritons in the AZO and lossy modes that exist due to the hyperbolic dispersion of the arrays. With the ability to remove these particles from their growth substrates, we were able to demonstrate that the arrays could be transferred to visibly transparent and mechanically flexible substrates while maintaining their broadband absorption in the NIR. We believe the synthetic strategies presented here are universal and can be applied to other nanoparticle systems. Not only would this enable a host of different materials that operate at distinct parts of the electromagnetic spectrum, but it is anticipated that novel light–matter interactions that have yet to be explored would be uncovered.

Materials and Methods

HNT Array Fabrication. HNT arrays were fabricated using silicon nanohole templates created by nanosphere lithography. Stöber particles (770-nm diameter) were grown from standard processes (33) and used as the nanosphere mask. Next, the Stöber particles were functionalized with 3-aminopropylmethyldiethoxysilane (APMDES), cleaned, and deposited onto p-type, double-sided polished, prime silicon using a Langmuir Blodgett trough. The silica particles were then shrunk using RIE with CHF_3 and Ar gases in an Oxford P80 (34). A 45-nm-thick nickel film was then deposited on the sample using a Temescal BJD 1800 electron beam evaporator. The Stöber particles were then mechanically removed with a Cleanroom Q-tip and sonication. Next, using an Oxford P100 with SF_6 and C_4F_8 gases, the exposed silicon was etched creating the nanohole template. After removing the nickel mask using TFB nickel etchant, the ZnO/AZO HMM was deposited into the nanoholes with a Beneq TFS200 ALD system operating at a reactor temperature of 185 or 200 °C. Diethylzinc, trimethylaluminum, and deionized water were used as the zinc, aluminum, and oxygen sources, respectively. The Zn:Al pulse ratio for the AZO films was kept constant at 20:1 for all experiments. The film thicknesses were first determined for each material on planar silicon substrates by ellipsometry using a Rudolph Auto EL ellipsometer at each deposition temperature. A total HMM thickness of ∼350 nm (each individual ZnO and AZO layer was 10 nm) was deposited on the nanohole template such that the nanoholes were completely sealed. Next, a 20-nm protection layer of HfO_2 was deposited via ALD by using tetrakis(dimethylamido)hafnium(IV) and water as the hafnium and oxygen sources, respectively. After depositing the HMM and protection layer, rapid thermal processing was carried out to activate the aluminum dopants (23) using an AG Associates Heat Pulse 610 with a 1.5 $L{\cdot}min^{-1}$ nitrogen flow rate. The top layers of HfO_2 and ZnO/AZO were then removed using RIE with CHF_3 and Ar gases using an Oxford P80 until the top silicon was exposed. The exposed silicon was removed using an Oxford P100 with SF_6 and C_4F_8 gases, leaving behind the HNT array (Fig. S1). The roughened HNTs were created by additional etching of the HNTs (deposited at a temperature of 200 °C) using RIE with CHF_3 and Ar gases. Before measurements, dilute HCl was applied to the back of the samples to remove any contaminates that may have been generated during the ALD process.

Numerical Simulations. Simulations of the exact structure were carried out using finite-difference time-domain (FDTD) methods (Lumerical), and EMA simulations were implemented with COMSOL using the finite-element method (FEM). All simulations used plane wave excitation with periodic boundary conditions at normal incidence. The optical constants used for AZO and ZnO were experimentally determined via ellipsometry as previously reported (23). TiN and (Al,Sc)N optical constants were obtained from literature (32). All structures were simulated in a vacuum without any substrate.

HNT Transfer Process. The HNT arrays were transferred to a flexible polymer film by depositing a ∼60-μm film of PDMS and etching away the silicon substrate. First, the PDMS film was coated on the top of the HNT array by spin coating at $8.5 \times g$ for 45 s and curing at 125 °C for 8 min. The back silicon was then cleaned with O_2 plasma (Oxford P100) and removed using a Xactix XeF_2 Etcher.

Optical Measurements and Imaging. All experimental absorption measurements between 1,200 and 2,400 nm were taken using a PerkinElmer Lambda 1050 UV/Vis/NIR spectrometer. For non–angle-dependent data, a 150-mm Spectralon-coated integrating sphere with a photomultiplier tube (visible wavelengths) and InGaAs (NIR wavelengths) detector was used. For angle-dependent measurements, a universal reflectance accessory was used with an InGaAs detector. IR reflectance was determined using a Bruker LUMOS Fourier transform IR (FTIR). All SEM imaging was carried out on a FEI XL30 ultrahigh-resolution microscope.

ACKNOWLEDGMENTS. We acknowledge Dr. Bernd Fruhberger, Larry Grissom, Ivan Harris, and Dr. Xuekun Lu of Calit2 at University of California, San Diego, for their support in installing and calibrating the necessary precursor lines in the ALD system and assistance. We also acknowledge the Basov Laboratory for allowing us to use their Bruker LUMOS FTIR. Funding for shared facilities used in this research was provided by the National Science Foundation (Award NSF CBET1236155).

1. Lenert A, et al. (2014) A nanophotonic solar thermophotovoltaic device. *Nat Nanotechnol* 9(2):126–130.
2. Wu C, et al. (2012) Metamaterial-based integrated plasmonic absorber/emitter for solar thermo-photovoltaic systems. *J Opt* 14(2):024005.
3. Liu X, et al. (2011) Taming the blackbody with infrared metamaterials as selective thermal emitters. *Phys Rev Lett* 107(4):045901.
4. Chen X, Chen Y, Yan M, Qiu M (2012) Nanosecond photothermal effects in plasmonic nanostructures. *ACS Nano* 6(3):2550–2557.
5. Shi H, Ok JG, Baac HW, Guo LJ (2011) Low density carbon nanotube forest as an index-matched and near perfect absorption coating. *Appl Phys Lett* 99(21):211103.
6. Nelms N, Dowson J (2005) Goldblack coating for thermal infrared detectors. *Sens Actuators A Phys* 120(2):403–407.
7. Mizuno K, et al. (2009) A black body absorber from vertically aligned single-walled carbon nanotubes. *Proc Natl Acad Sci USA* 106(15):6044–6047.
8. Li W, et al. (2014) Refractory plasmonics with titanium nitride: Broadband metamaterial absorber. *Adv Mater* 26(47):7959–7965.

9. Ferrari L, Wu C, Lepage D, Zhang X, Liu Z (2015) Hyperbolic metamaterials and their applications. *Prog Quant Electron* 40:1–40.
10. Poddubny A, Iorsh I, Belov P, Kivshar Y (2013) Hyperbolic metamaterials. *Nat Photon* 7(12):948–957.
11. Hoffman AJ, et al. (2007) Negative refraction in semiconductor metamaterials. *Nat Mater* 6(12):946–950.
12. Naik GV, Liu J, Kildishev AV, Shalaev VM, Boltasseva A (2012) Demonstration of Al:ZnO as a plasmonic component for near-infrared metamaterials. *Proc Natl Acad Sci USA* 109(23):8834–8838.
13. Yao J, et al. (2008) Optical negative refraction in bulk metamaterials of nanowires. *Science* 321(5891):930.
14. Lu D, Kan JJ, Fullerton EE, Liu Z (2014) Enhancing spontaneous emission rates of molecules using nanopatterned multilayer hyperbolic metamaterials. *Nat Nanotechnol* 9(1):48–53.
15. Liu Z, Lee H, Xiong Y, Sun C, Zhang X (2007) Far-field optical hyperlens magnifying sub-diffraction-limited objects. *Science* 315(5819):1686.
16. Narimanov EE, Li H, Barnakov YA, Noginov MA (2010) Darker than black: Radiation-absorbing metamaterial. *Proceedings of the Lasers and Electro-Optics/Quantum Electronics and Laser Science Conference: 2010 Laser Science to Photonic Applications (CLEO/QELS'10)* (Optical Society of America, San Jose, CA), QPDA6.
17. Narimanov EE, Li H, Barnakov YA, Tumkur TU, Noginov MA (2013) Reduced reflection from roughened hyperbolic metamaterial. *Opt Express* 21(12):14956–14961.
18. Cui Y, et al. (2012) Ultrabroadband light absorption by a sawtooth anisotropic metamaterial slab. *Nano Lett* 12(3):1443–1447.
19. Ji D, et al. (2014) Broadband absorption engineering of hyperbolic metafilm patterns. *Sci Rep* 4:4498.
20. Zhou J, Kaplan AF, Chen L, Guo LJ (2014) Experiment and theory of the broadband absorption by a tapered hyperbolic metamaterial array. *ACS Photonics* 1(7):618–624.
21. Jiang CY, et al. (2008) High-bendability flexible dye-sensitized solar cell with a nanoparticle-modified ZnO-nanowire electrode. *Appl Phys Lett* 92:143101.
22. McAlpine MC, Ahmad H, Wang D, Heath JR (2007) Highly ordered nanowire arrays on plastic substrates for ultrasensitive flexible chemical sensors. *Nat Mater* 6(5):379–384.
23. Riley CT, et al. (2016) High-quality, ultraconformal aluminum-doped zinc oxide nanoplasmonic and hyperbolic metamaterials. *Small* 12(7):892–901.
24. Gong SC, et al. (2013) Aluminum-doped zinc oxide formed by atomic layer deposition for use as anodes in organic light emitting diodes. *J Vac Sci Technol A* 31(1):01A101.
25. Dhakal T, et al. (2012) Growth morphology and electrical/optical properties of Al-doped ZnO thin films grown by atomic layer deposition. *J Vac Sci Technol A* 30(2): 021202.
26. Riley CT, et al. (2014) Plasmonic tuning of aluminum doped zinc oxide nanostructures by atomic layer deposition. *Phys Status Solidi Rapid Res Lett* 8(11):948–952.
27. Dasgupta NP, et al. (2010) Atomic layer deposition of Al-doped ZnO films: Effect of grain orientation on conductivity. *Chem Mater* 22(16):4769–4775.
28. Narimanov EE (2014) Photonic hypercrystals. *Phys Rev X* 4(4):041014.
29. Galfsky T, Narimanov EE, Menon VM (2015) Enhanced spontaneous emission in photonic hypercrystals. *Frontiers in Optics* (Optical Society of America, Washington, DC), FW6A.3.
30. Zhang Y, et al. (2013) Zhang M, Ge C, Lu M, Zhang Z, Cunningham BT (2013) A self-referencing biosensor based upon a dual-mode external cavity laser. *Appl Phys Lett* 102(21):213701.
31. Liu J, et al. (2014) Optical absorption of hyperbolic metamaterial with stochastic surfaces. *Opt Express* 22(8):8893–8901.
32. Naik GV, et al. (2014) Epitaxial superlattices with titanium nitride as a plasmonic component for optical hyperbolic metamaterials. *Proc Natl Acad Sci USA* 111(21): 7546–7551.
33. Stöber W, Fink A, Bohn E (1968) Controlled growth of monodisperse silica spheres in the micron range. *J Colloid Interface Sci* 26(1):62–69.
34. Hsu C-M, Connor ST, Tang MX, Cui Y (2008) Wafer-scale silicon nanopillars and nanocones by Langmuir-Blodgett assembly and etching. *Appl Phys Lett* 93(13): 133109.
35. Smith EJ, Liu Z, Mei Y, Schmidt OG (2010) Combined surface plasmon and classical waveguiding through metamaterial fiber design. *Nano Lett* 10(1):1–5.
36. Avrutsky I, Salakhutdinov I, Elser J, Podolskiy V (2007) Highly confined optical modes in nanoscale metal-dielectric multilayers. *Phys Rev B* 75(24):241402.
37. Prather DW, Shi S, Sharkwawy A, Murakowski J, Schneider G (2009) Numerical methods. *Photonic Crystals: Theory, Applications, and Fabrication* (Wiley, Hoboken, NJ), pp 63–131.
38. Yeh P (1979) Electromagnetic propagation in birefringent layered media. *J Opt Soc Am* 69:742–756.
39. Cojocaru E (2000) Forbidden gaps in periodic anisotropic layered media. *Appl Opt* 39(25):4641–4648.
40. Boucher YG, Le Rouzo J, Ribet-Mohamed I, Haïdar R (2008) Modified form birefringence in periodic multilayer structures including uniaxial anisotropic materials. *J Opt Soc Am B* 25:777–784.
41. Rytov SM (1956) Electromagnetic properties of a finely stratified medium. *J Exp Theor Phys* 2:466–475.
42. Podolskiy V (2012) Anisotropic and hyperbolic metamaterials. *Tutorials in Metamaterials*, eds Noginov M, Podolskiy V (CRC, Boca Raton, FL), pp 163–207.
43. Tumkur TU, et al. (2012) Control of reflectance and transmittance in scattering and curvilinear hyperbolic metamaterials. *Appl Phys Lett* 101(9):091105.